# Enhanced Electroresponsive Performance of Double-Shell $SiO_2/TiO_2$ Hollow Nanoparticles

**Seungae Lee,‡ Jungsup Lee,‡ Sun Hye Hwang, Juyoung Yun, and Jyongsik Jang***

School of Chemical and Biological Engineering, Seoul National University, 599 Gwanak-ro, Gwanak-gu, Seoul 151-742, Korea. ‡These authors (S.L. and J.L.) contributed equally to this work.

**ABSTRACT** The double-shell $SiO_2/TiO_2$ hollow nanoparticles (DS HNPs) are successfully fabricated and adopted as dispersing materials for electrorheological (ER) fluids to investigate an influence of shell structure on ER properties. The DS HNPs-based ER fluid exhibits outstanding ER performance which is 4.1-fold higher compared to that of single shell $SiO_2/TiO_2$ hollow nanoparticles (SS HNPs)-based ER fluid. The significantly improved ER property of DS HNPs-based ER fluid is ascribed to the enhanced interfacial polarization. In addition, the ER activities of DS HNPs-based ER fluids are examined depending on the particle diameter. The yield stress of DS HNPs-based ER fluids increases up to 302.4 kPa under an electric field of 3 kV $mm^{-1}$ by reducing the particle size, which is remarkable performance enough to promise sufficient probability for practical and industrial applications. The enhanced ER performance of the smaller DS HNPs is attributed to the increased surface area of large pores (30−35 nm) within the shells, resulting in a large achievable polarizability determined by dielectric constants. Furthermore, the antisedimentation property is analyzed in order to offer an additional insight into the effect of particle size on the ER fluids.

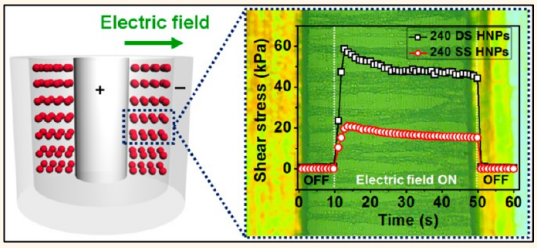


**KEYWORDS:** electrorheological response · hollow nanoparticles · double shell · silica · titania

Electrorheological (ER) fluids, colloidal suspensions of polarizable particles dispersed in insulating liquid medium, self-assemble to construct aligned fibril structures under an applied electric field. These fluids have attracted considerable attention in various fields because of their distinguishing features, such as low power consumption, fast response time, reversibility, and simple mechanics.[1−3] However, there are still several limitations for commercialization of ER fluids because of relatively low polarization force and particle sedimentation.

To overcome these limitations and facilitate the commercialization, various types of materials have been introduced as ER materials. For instance, polymer/inorganic hybrid materials were used because of their high polarization force attributed to the difference in chemical structure between polymer and inorganic material.[4] In addition, metal-doped titanium oxide was utilized as an ER material and showed high interparticle interaction and interfacial polarization ascribed to its high active surface area.[5] Moreover, core−shell-structured materials were widely used in ER fluids to utilize the features of both core and shell materials.[6] Among these various materials, the hollow structure has received considerable attention from researchers because of its high polarization force and high dispersity, which enables the ER materials to exhibit high performance. For example, Quadrat *et al.* synthesized polypyrrole-coated $TiO_2$ hollow nanoparticles that showed enhanced ER properties through increased active surface area.[7] In addition, Sung *et al.* employed polyaniline hollow particles with low-density as an ER material to reduce the sedimentation problem.[8] Furthermore, Cheng *et al.* improved the ER performance of hollow structures with a large surface area by growing a $TiO_2$ branch on the $TiO_2$ hollow sphere.[9] Although many approaches have been proposed, previous researches on hollow structures as ER materials were limited to utilization of single-shell hollow nanoparticles. Accordingly, a more in-depth study is required to clarify the influence of particle structure on ER

* Address correspondence to jsjang@plaza.snu.ac.kr.

Received for review December 2, 2014 and accepted April 6, 2015.

**Published online April 06, 2015**
**10.1021/nn5068495**

activities for a better understanding of the mechanism underlying the ER effect.

Herein, we scrutinize the ER properties depending on the shell structure of a particle by fabricating double-shell $SiO_2/TiO_2$ hollow nanoparticles (DS HNPs) and applying the DS HNPs as ER materials. To the best of our knowledge, this is the first attempt to employ double-shell-structured hollow nanoparticles in ER fluid so far reported. In addition, the influence of pore structure and distribution on ER performance is analyzed for single shell $SiO_2/TiO_2$ hollow nanoparticles (SS HNPs) and DS HNPs. Furthermore, ER activities of four different-sized DS HNPs-based ER fluids are investigated in order to gain an insight into the effect of particle size on the ER fluids. Moreover, dielectric parameters and the antisedimentation property of the prepared ER fluids are measured to confirm the enhanced ER performance of the double-shell hollow structures.

## RESULTS AND DISCUSSION

**Fabrication of Size-Controlled Double-Shell $SiO_2/TiO_2$ Hollow Nanoparticles.** The formation procedure of the DS HNPs was illustrated in Figure 1. First, silica nanoparticles, which act as core template, were prepared using the Stöber method. The $TiO_2$ shell was coated on the silica core template by the sol−gel method using titanium(IV) isopropoxide (TTIP) as precursor. Polyvinylpyrrolidone (PVP) was adsorbed on the synthesized $SiO_2/TiO_2$ core/shell nanoparticles (ST CS NPs) to increase affinity between the $TiO_2$ shell and the $SiO_2$ precursor. Hydroxyl groups in oxide surfaces interact with negatively charged carbonyl groups of the PVP, leading to enhanced affinity. TEOS was dropped to coat the $SiO_2$ layer on the ST CS NPs, resulting in $SiO_2/TiO_2/SiO_2$ core/shell nanoparticles (STS CS NPs). $SiO_2/TiO_2/SiO_2/TiO_2$ core/shell nanoparticles (STST CS NPs) were synthesized *via* the sol−gel reaction by adding TTIP in the solution of STS CS NPs. Finally, to obtain DS HNPs, STST CS NPs were etched by sonication with $NH_4OH$.

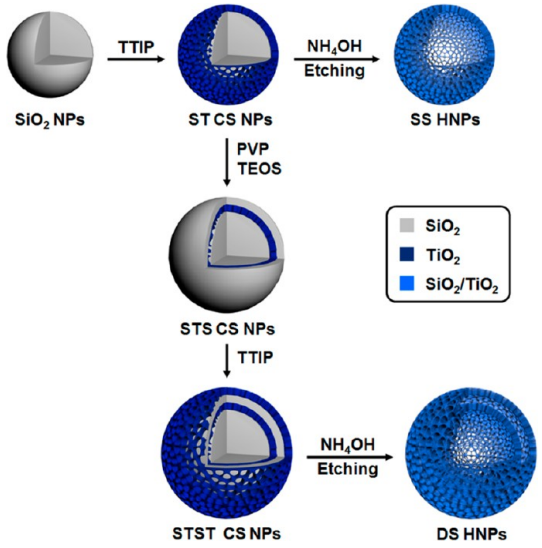


**Figure 1. Schematic illustration of the formation procedure of DS HNPs with a highly porous structure *via* PVP adsorption on the $TiO_2$, sol−gel reaction, and etching process.**

Uniform single shell $SiO_2/TiO_2$ hollow nanoparticles (SS HNP) and double-shell $SiO_2/TiO_2$ hollow nanoparticle (DS HNP) with a diameter of 240 nm were successfully fabricated (Figure 2a,b). The SS HNPs could be fabricated using a method similar to that of the DS HNPs, except that ST CS NPs were etched instead of STST CS NPs. For the fabrication of the SS HNPs, 150 nm-sized silica particles were used as a core template. It was confirmed that the shell thickness of SS HNP was *ca.* 57 nm as shown in Figure 2a. The DS HNP with same size has the inner and outer shell thicknesses of 27 and 34 nm, respectively (Figure 2b). The shell thickness of SS HNPs and DS HNPs can be controlled by adjusting the amount of TTIP and TEOS during the fabrication procedure.

The size of DS HNPs was controlled by 120, 150, 180, and 240 nm by using different-sized silica core templates (Figure 2c−f). The sizes of the silica core templates utilized for the fabrication of 120, 150, 180, and 240 nm-sized DS HNPs were 40, 60, 80, and 120 nm, respectively. Both inner and outer shell thicknesses of DS HNPs increased with increasing size of DS HNPs as described in Table 1. As stated above, shell thicknesses of DS HNPs can be adjusted by using different amounts of TTIP and TEOS. However, an excess amount of TTIP and TEOS causes an adherence of inner and outer shells, resulting in a thick single shell.

The elemental composition of the SS HNP and four different-sized (120, 150, 180, and 240 nm) DS HNPs were acquired by elemental analyzer (EA) and inductively coupled plasma-atomic emission spectrometer (ICP-AES). Judging from the results of elemental analysis, the final products, that is, the SS HNPs and the four different-sized DS HNPs, contain a small amount of organic materials. These organic materials are residues of PVP and $NH_4OH$ which were used for the formation of $SiO_2$ shell and etching process, respectively. However, it is considered that the residual organic materials did not affect the ER performance because the amount of the residues was very small. Moreover, since the contents of C, H, and N were similar in the SS HNPs and the four different-sized DS HNPs, the difference of ER performance was not ascribed to the residual organic materials. From the elemental analysis using ICP-AES, the contents of each element including Si and Ti were acquired as described in Supporting Information, Table S1. Furthermore, the elemental mapping images were obtained by scanning transmission electron microscopy (STEM)-energy dispersive spectroscopy (EDS) to visually identify the elemental distribution of the SS HNP and the DS HNPs (Figure 3).

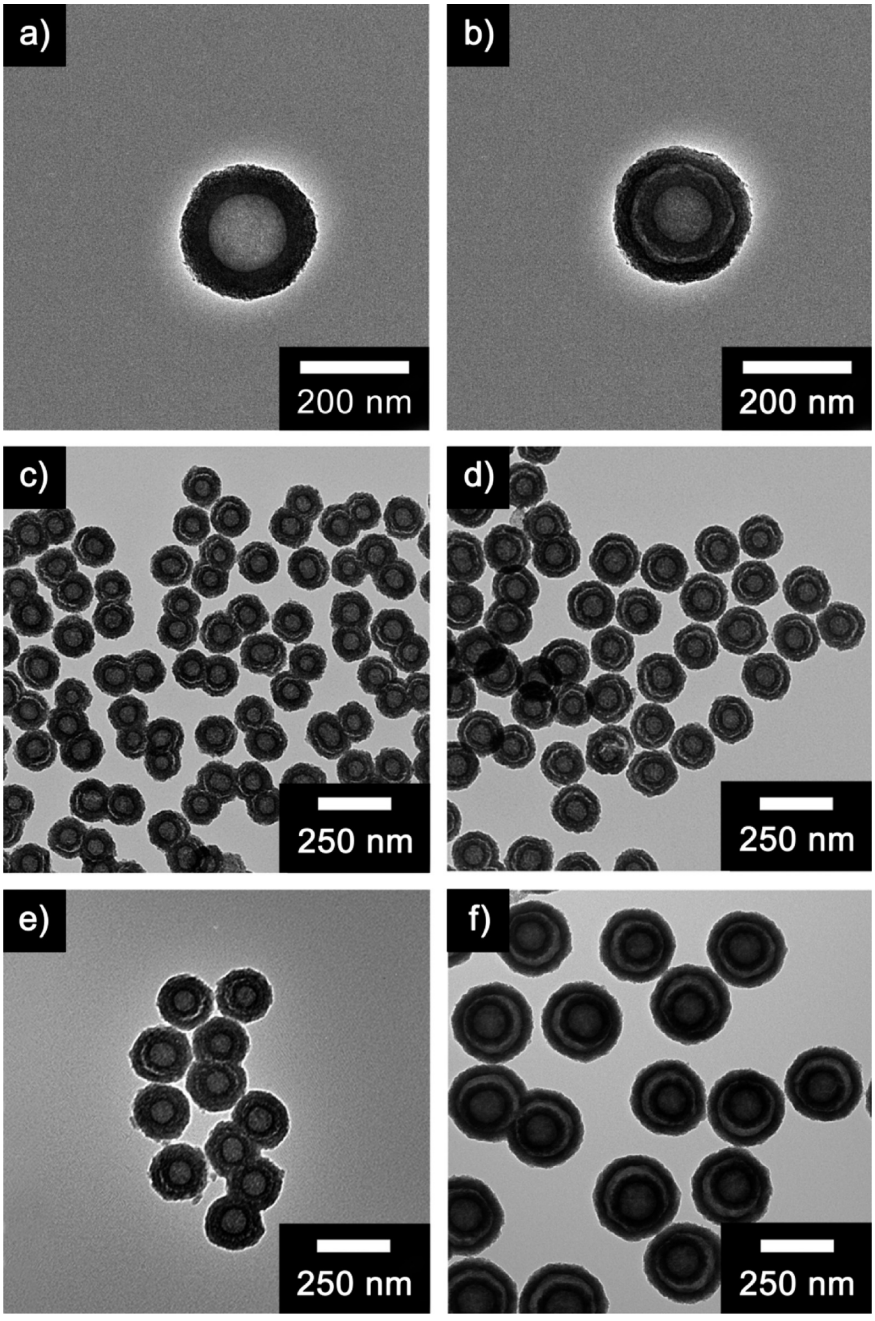


**Figure 2. Transmission electron microscopy (TEM) images of (a) single shell $SiO_2/TiO_2$ hollow nanoparticle (SS HNP) and (b) double-shell $SiO_2/TiO_2$ hollow nanoparticle (DS HNP) with a diameter of 240 nm. TEM images of DS HNPs with a diameter of (c) 120, (d) 150, (e) 180, and (f) 240 nm.**

**TABLE 1. Inner and Outer Shell Thicknesses of Four Different-Sized DS HNPs**

| | inner shell thickness[a] | outer shell thickness[a] |
|---|---|---|
| samples | nm | nm |
| 120 nm DS HNPs | 10.8 ± 5 | 13.5 ± 5 |
| 150 nm DS HNPs | 13.5 ± 5 | 16.9 ± 5 |
| 180 nm DS HNPs | 19.9 ± 5 | 24.9 ± 5 |
| 240 nm DS HNPs | 27.1 ± 5 | 33.9 ± 5 |

[a] The average thicknesses were confirmed by TEM (50 particles counted).

**Influence of the Number of $SiO_2/TiO_2$ Shell on Electrorheological Properties.** To investigate the influence of the number of shells on ER performances, the SS HNP-based ER fluid and the DS HNP-based ER fluid were prepared by dispersing the dried particles in silicone oil, a dispersing media. As shown in Figure 4a, variations of both shear stress and viscosity were examined as a function of the shear rate under 3 kV $mm^{-1}$ of electric field strength. The leakage current of the SS HNPs and the DS HNPs was 0.010 and 0.012 mA, respectively, under 3 kV $mm^{-1}$ of electric field. In the

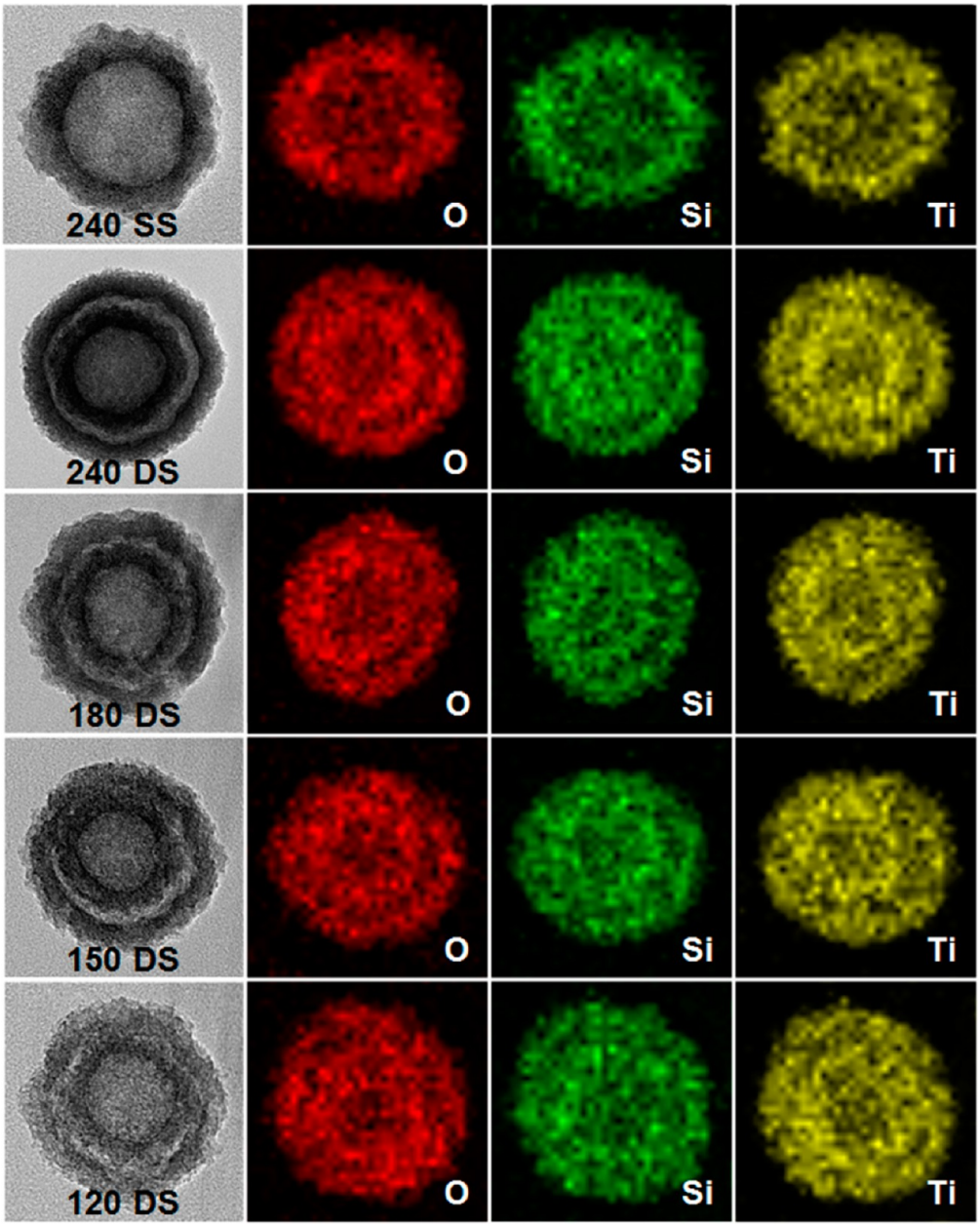


**Figure 3. STEM-elemental-mapping images of 240 nm-sized single shell $SiO_2/TiO_2$ hollow nanoparticle (SS HNP) and four different-sized (240, 180, 150 and 120 nm) double-shell $SiO_2/TiO_2$ hollow nanoparticles (DS HNPs).**

case of 240 nm-sized DS HNPs-based ER fluid, the plateau region was generated at the low shear rate region due to the competition between induced electrostatic interaction of particles and hydrodynamic force by shear flow, which represents typical Bingham plastic behavior.[10−12] At the end of plateau region, critical shear rate, the shear stress increased gradually, which is identical to typical Newtonian fluid behavior.[13,14] Alternately, in the case of SS HNPs-based ER fluid, the shear stress decreased as the shear rate increased approaching to a minimum shear stress at a critical shear rate. To cover the shear stress decrease phenomenon at the low shear rate region, a modified theology equation called the Cho−Choi−Jhon (CCJ) model was provided as follows:

$$\tau = \frac{\tau_y}{1+(t_1\dot{\gamma})^{\alpha}} + \eta_{\infty}\left(1+\frac{1}{(t_2\dot{\gamma})^{\beta}}\right)\dot{\gamma}$$

where $\tau$ is the shear stress, $\tau_y$ is the dynamic yield stress, $\dot{\gamma}$ is the shear rate, $t_1$ and $t_2$ are time constants, $\eta_{\infty}$ is the viscosity at infinite shear rate, and the exponent $\alpha$ is associated to the decrease of shear stress at a low shear rate region, whereas $\beta$ is for the high shear rate region ($0 < \beta \leq 1$).[15,16] Because of the relatively weak electrostatic interactions between the particles, the decrease of shear stress was observed for the SS HNPs-based ER fluid, which is analogous with the CCJ model. Moreover, the viscosity of ER fluids decreased as the

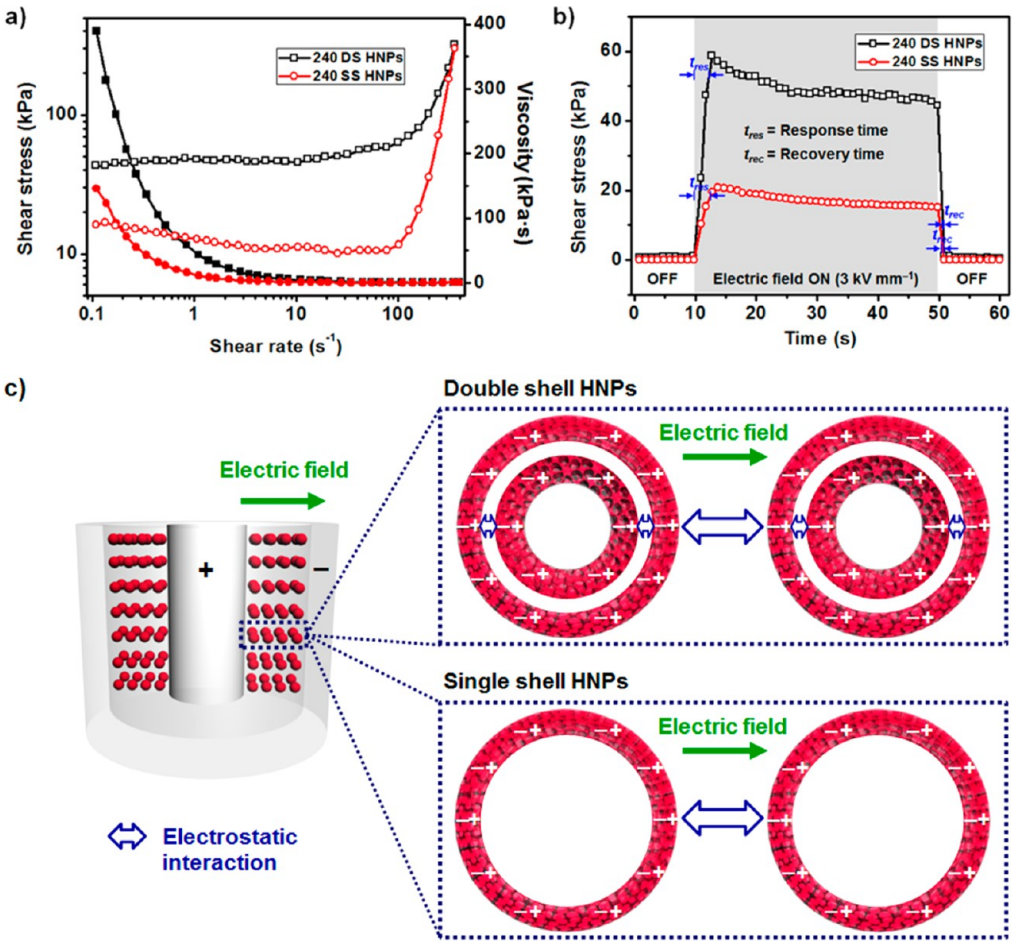


**Figure 4. (a) Shear stress (open symbol) and viscosity (closed symbol) of 240 nm-sized single shell $SiO_2/TiO_2$ hollow nanoparticles (240 SS HNPs)-based ER fluid and 240 nm-sized double-shell $SiO_2/TiO_2$ hollow nanoparticles (240 DS HNPs)-based ER fluid (10 wt% in silicone oil) under 3 kV mm$^{-1}$ of electric field. (b) Effect of switching the electric field on shear stress. The shear rate was 0.1 s$^{-1}$. (c) Schematic illustration for the polarization behavior of DS HNPs and SS HNPs under an applied electric field.**

shear rate increased, which represents shear thinning behavior. Judging from the value of yield stress, the DS HNP-based ER fluid exhibited approximately 4.1 times higher yield stress than the SS HNP-based ER fluid.

To examine the reproducibility of ER fluids, the shear stress was measured during the electric field on and off (Figure 4b). The reproducibility can be verified by the response time and recovery time, which is defined as the time required for reaching 90% of its final value.[17] It was confirmed that the DS HNP-based ER fluid represented faster response and recovery time than the SS HNP-based ER fluid.

The schematic illustration for explanation on the effect of the number of $SiO_2/TiO_2$ shell was provided in Figure 4c. When an external electric field was applied in the fluid, the polarization was generated on the ER particles along the electric field direction. Because of the generated polarization, the particles formed a fibrillar structure along the electric field direction by the induced electrostatic interaction between the dispersed ER particles. In the case of the DS HNP-based ER fluid, additional electrostatic interactions were formed between the two shells in the particle, which caused stronger shear stress. The high surface area in DS HNPs achieved by increasing the number of shells produced the interfacial polarizability under an applied electric field, resulting in the enhancement of ER performance. In other words, more surface sites for charge accumulation were produced because of the high surface area additionally formed by the inner cavity of DS HNPs, which associated with strong particle polarization.[18] Accordingly, the DS HNPs-based ER fluid exhibited higher ER performance than the SS HNPs-based ER fluid.

The structural change under the electric field on and off was observed by optical microscope (Figure 5). When the electric field was switched on, the ER particles dispersed randomly forming a fibril structure within a few tens of milliseconds.

**Electrorheological Activities of Double-Shell $SiO_2/TiO_2$ Hollow Nanoparticles Depending on Particle Size.** To gain in-depth insight into the size effect of ER materials, four different-sized (120, 150, 180, and 240 nm) DS HNP-based ER fluids were prepared for analysis of ER activities.

The variations of both shear stress and viscosity depending on the shear rate were measured under 3 kV $mm^{-1}$ of electric field strength. The leakage current of the 120, 150, 180 and 240 nm-sized DS HNPs-based ER fluids was 0.036, 0.028, 0.022, and 0.012 mA, respectively, under 3 kV $mm^{-1}$ of electric field. As shown in Figure 6a, all ER fluids except 120 nm-sized DS HNPs-based ER fluid exhibited the typical Bingham plastic behavior below the critical shear rate and the typical Newtonian fluid behavior beyond the critical shear rate. In the case of the 120 nm-sized DS HNPs-based ER fluid, the shear stress slightly decreased with increasing the shear rate at low shear rate region, which is corresponding to the CCJ model. Since the 120 nm-sized DS HNPs had relatively low density compared with other DS HNPs, it was more difficult for the 120 nm-sized DS HNPs to sustain their fibril-like structure against the hydrodynamic force.

In particular, yield stress was enhanced with a decreasing diameter of the particle, which was attributed to the high mobility and high external surface area of a small-sized particle. The yield stress of 120 nm-sized DS HNPs-based ER fluid was approximately 7.6 times higher than that of 240 nm-sized DS HNPs-based ER fluid. Particularly, 120, 150, and 180 nm-sized DS HNPs-based ER fluids exhibited yield stress beyond 130 kPa, which corresponded to the giant electrorheological (GER) fluids. The GER fluids are set apart from the conventional ER fluids because the yield stress of GER fluids exceeds the theoretical upper bound.[19] One of the most popular theories for explaning the mechanism of ER fluid under an electric field is the polarization model (conventional ER fluid mechanism).[20] In the polarization model, yield stress is ascribed to the formation of a fibril-like structure by the electrostatic interactions between the particles and the Maxwell–Wagner interfacial polarization. The induced electrostatic force is dependent on the dielectric constant mismatch between the solid particles and dispersing medium. The relationship between the yield stress ($\tau_y$) and an applied electric field strength ($E_0$) can be elucidated using the

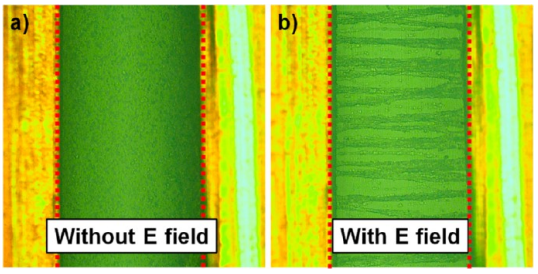


**Figure 5. Optical microscope images of DS HNPs-based ER fluid (a) without an electric field and (b) under an electric field. The gap distance between two electrodes was adjusted to 1 mm.**

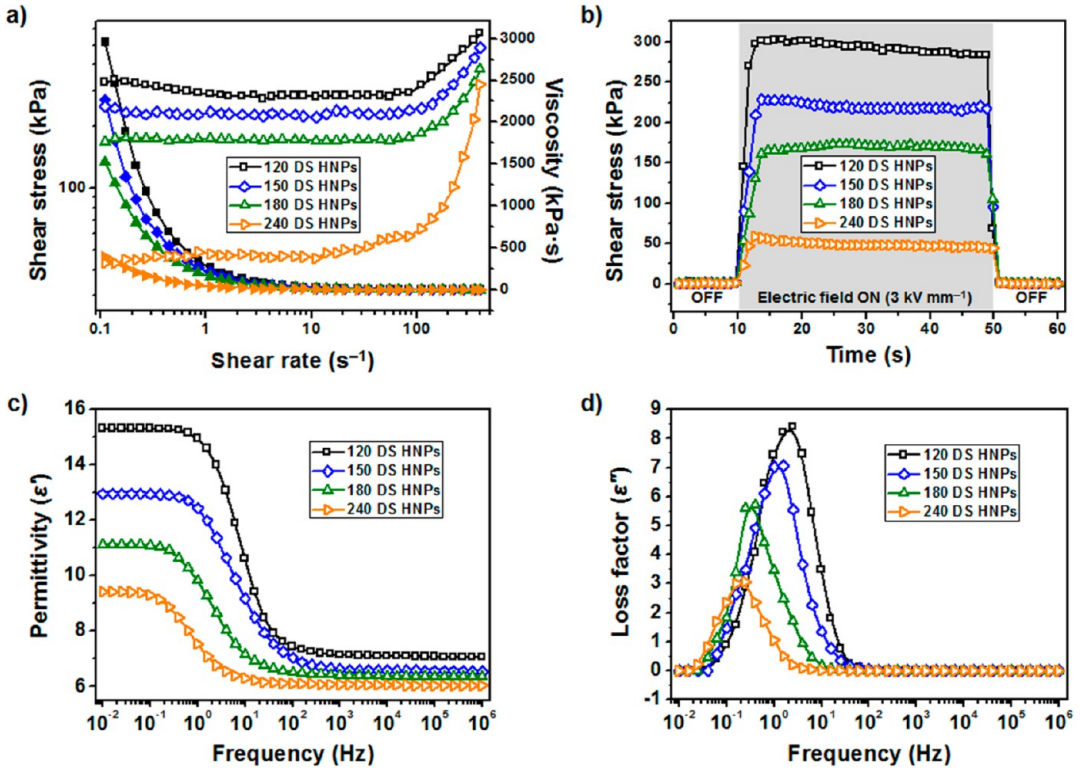


**Figure 6. (a) Shear stress (open symbol) and viscosity (closed symbol) of four different-sized (120, 150, 180, 240 nm) DS HNPs-based ER fluid (10 wt% in silicone oil) under 3 kV $mm^{-1}$ of electric field. (b) Effect of switching the electric field on shear stress. The shear rate was 0.1 $s^{-1}$. (c) Permittivity ($\varepsilon'$) and (d) loss factor ($\varepsilon''$) as a function of electric field frequency for four different-sized (120, 150, 180, 240 nm) DS HNPs-based ER fluids (10 wt% in silicone oil).**

following point-dipole approximation:

$$\tau_y \propto \varphi K_f E_0^2 f(\beta)$$

where $\varphi$ is the volume fraction of particles, $\beta$ is the dimensionless dielectric mismatch parameter ($\beta = (K_p - K_f)/(K_p + 2K_f)$). Here, $K_p$ and $K_f$ are the dielectric permittivity of particles and fluid, respectively.[21] However, in some systems especially under high electric field strength, the behavior of fluid does not follow the polarization model. The conduction model elucidates particle interactions after the chain-like structure formation, irrespective of the microstructural changes when an electric field is turned on. In the conduction model, the yield stress is proportional to the applied electric field strength to the power of 1.5 ($\tau_y \propto E_0^{3/2}$), which is ascribed to the nonlinear conductivity effect caused by the electrical breakdown of fluids.[22] Although several models have been provided to account for the behavior of ER fluids, these models have some limit to include the behavior of GER fluids. Huang *et al.* proposed the surface polarization layer model based on their experimental observation.[23,24] In the surface polarization layer model, it is a crucial element that the surface dipoles form two aligned layers in the contact region. The aligned dipole layers generate an electrostatic force which is holding the two particles together. By the equilibrium of the electrostatic force and the elastic force between the neighboring particles, the overlap of two particles is determined. According to this model, the yield stress is referred to as the shear stress at which the two neighboring particles irreversibly lose contact.

The fast response and reproducibility of small-sized DS HNP-based ER fluid were confirmed by measuring shear stress under the electric field on and off (Figure 6b). The small-sized DS HNP-based ER fluid represented more enhanced shear stress and faster response and recovery time than the ER fluid having relatively large-sized particles. These phenomena resulted from the synergistic effect of higher mobility and higher external surface area from the small-sized diameter.[25]

Total surface area ($A_{BET}$) and pore distribution of the fabricated DS HNPs were directly obtained from Brunauer–Emmett–Teller (BET) analysis (Table 2). Additionally, surface area of the small pores within shells ($A_{ISP}$) and the surface of the shells except small pores within shells ($A_{shell}$) were calculated in order to analyze the relationship between surface area and ER properties using the formula[26]

$$A_{shell} = 3V_{SiO_2/TiO_2}(R^2 + r^2)/(R^3 - r^3)$$

$$A_{BET} = A_{ISP} + A_{shell}$$

where $V_{SiO_2/TiO_2}$ (= 0.333 $cm^3\ g^{-1}$) is the specific volume of the $SiO_2/TiO_2$ composites, and $R$ and $r$ represent the outer and inner radius of the shell, respectively. $A_{BET}$ increased with increasing size of the DS HNPs, reaching 497 $m^2\ g^{-1}$ at 240 nm. The DS HNPs contain small pores (size, 3–4 nm) and large pores (size, 30–35 nm) formed in the intrashell and inner cavity, respectively. At the initial stage of the etching process, silica in the titania/silica interface is first etched out but not titania. With continuous etching under sonication, high intensity energy arises from the cavity between silica and titania made at the initial stage. Therefore, corrosion of both titania and silica occurs under the stringent conditions.[27] The etched fragments of titania and silica are released and diffused to the titania shell layer. Subsequently, these fragments of titania and silica condensate and redeposit on the titania shell by Ostwald ripening.[28,29] Consequently, small pores (size, 3–4 nm) and large pores (size, 30–35 nm) are formed in the intrashell and inner cavity, respectively, as a result of the sonication-mediated etching and redeposition process. The ratio of small pores to large pores increased with the increasing size of DS HNPs, which indicates that more intrashell pores exist in bigger sizes of DS HNPs (Supporting Information, Figure S1). Therefore, the DS HNPs with a diameter of 240 nm exhibited the largest $A_{BET}$ due to the large $A_{ISP}$ generated by the small pores within thicker shells of the DS HNPs. However, small pores within shells have little effect on enhancing ER properties because the polarization derived by large pores formed in the inner cavity is stronger than the polarization derived by small pores within the shell under an applied electric field. In other words, charge accumulation occurs more readily in surface sites formed by large pores than in those formed by small pores. Consequently, the surface area of the shell, except small pores within shells ($A_{shell}$), plays a critical role in enhancing ER properties by increasing the interfacial polarizability of particles. Among the fabricated DS HNPs with different diameters, 120 nm-sized DS HNPs (120 DS HNPs) exhibited the highest $A_{shell}$ of 112 $m^2\ g^{-1}$, which means 120 DS HNPs tends to polarize more easily under an applied electric field.

**TABLE 2. Brunauer–Emmett–Teller (BET) Analysis of Four Different-Sized (120, 150, 180, and 240 nm) DS HNPs for Measurement of Surface Area and Volume Ratio of Small Pores (3–4 nm) and Large Pores (30–35 nm) in DS HNPs.**

| samples | $A_{BET}$[a] $m^2\ g^{-1}$ | $A_{shell}$[b] $m^2\ g^{-1}$ | $A_{ISP}$[c] $m^2\ g^{-1}$ | small pore % | large pore % |
|---|---|---|---|---|---|
| 120 DS HNPs | 317 | 112 | 205 | 36 | 64 |
| 150 DS HNPs | 351 | 89.0 | 262 | 49 | 51 |
| 180 DS HNPs | 366 | 63.0 | 303 | 55 | 45 |
| 240 DS HNPs | 497 | 45.0 | 452 | 85 | 15 |

[a] $A_{BET}$: total surface area. [b] $A_{shell}$: surface area of the shell except small pores within shells. [c] $A_{ISP}$: surface area of the small pores within shells.

**TABLE 3. Dielectric Parameters for DS HNPs-Based ER Fluids[a]**

| particle size (nm) | $\varepsilon_0$ | $\varepsilon_\infty$ | $\Delta\varepsilon = \varepsilon_0 - \varepsilon_\infty$ | $f_{max}$[b] (Hz) | $\lambda$[c] (s) |
|---|---|---|---|---|---|
| 120 | 15.30 | 7.06 | 8.24 | 2.05 | 0.0776 |
| 150 | 12.95 | 6.55 | 6.40 | 1.24 | 0.128 |
| 180 | 11.12 | 6.36 | 4.76 | 0.343 | 0.464 |
| 240 | 9.42 | 6.04 | 3.38 | 0.209 | 0.762 |

[a] Dielectric parameters were examined by an impedance analyzer (1260, Solartron) with a dielectric interface (1296, Solartron). [b] The local frequency of the peak on the dielectric loss factor $\varepsilon''$ and the $f_{max}$ values were measured by nonlinear regression analysis using OriginPro. [c] The relaxation time, denoted by $\lambda = 1/(2\pi f_{max})$ ($f_{max}$ is the frequency of the loss peak).

In addition, the dielectric properties of ER materials are associated with ER activities due to the orientational polarization (Debye polarization) and interfacial polarization (Wagner polarization) generated under an electric field.[30,31] To examine the effect of dielectric properties of ER materials on ER performance, permittivity, and loss factor were measured as a function of the electric field frequency (Figure 6c,d). The plotted lines in Figure 6c,d were acquired by the following equation:

$$\varepsilon^* = \varepsilon' + i\varepsilon'' = \varepsilon_\infty + \frac{\Delta\varepsilon}{\{1 + (i\omega\lambda)^{1-\alpha}\}^\beta}$$

where $\varepsilon'$ is the dielectric constant, $\varepsilon''$ is the dielectric loss factor, $\varepsilon_0$ is the static permittivity ($\varepsilon_0 = \lim_{\omega \to 0} \varepsilon^*(\omega)$), $\varepsilon_\infty$ is the fictitious permittivity ($\varepsilon_\infty = \lim_{\omega \to \infty} \varepsilon^*(\omega)$), $\Delta\varepsilon$ is the polarizability ($\Delta\varepsilon = \varepsilon_0 - \varepsilon_\infty$), $\omega$ is the angular frequency, and $\lambda$ is the characteristic relaxation time of the medium. The exponents $\alpha$ and $\beta$ indicate the asymmetry and broadness of the corresponding spectra, respectively.[32,33] The specific values of dielectric parameters for DS HNP-based ER fluids were described in Table 3. The smaller DS HNPs-based ER fluid exhibits larger polarizability, which is associated with the strong particle polarization.[34,35] This phenomenon can be explained by higher surface area of the shell except small pores within shells in the smaller DS HNPs because the high surface area of the shell except small pores within shells can produce more surface sites for charge carrier accumulation.[36,37] Moreover, the relaxation times ($\lambda$) which is related to the interfacial polarization are estimated by the following equation:

$$\lambda = \frac{1}{2\pi f_{max}}$$

where $f_{max}$ is the frequency at maximum dielectric loss factor.[38,39] The relaxation time significantly decreased as the diameter of DS HNPs was reduced. In other words, the smaller DS HNPs-based ER fluid represented the faster polarization rate than the larger DS HNPs-based ER fluid.

The yield stress of ER fluids was measured depending on the temperature under a zero field condition

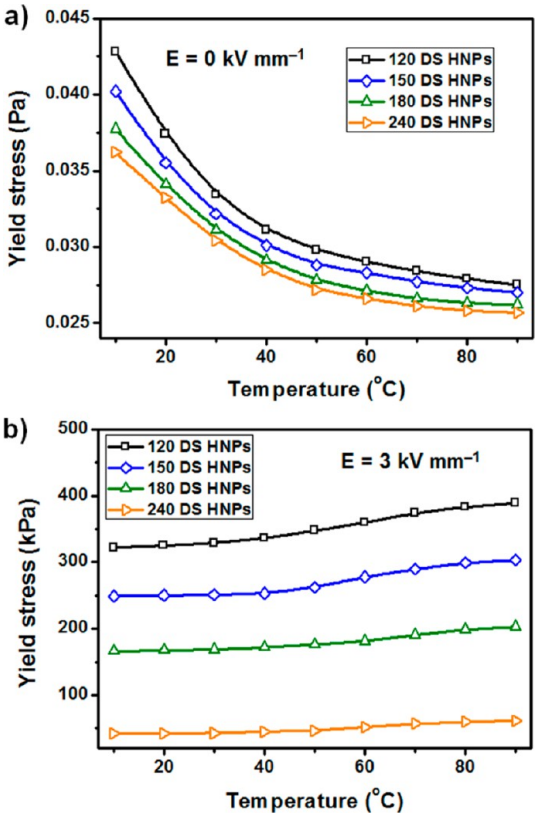


**Figure 7. Yield stress of four different-sized (120, 150, 180 and 240 nm) double-shell $SiO_2/TiO_2$ hollow nanoparticles (DS HNPs)-based ER fluids (10 wt% in silicone oil) (a) without an electric field and (b) under an electric field of 3 kV mm$^{-1}$.**

(Figure 7a). Yield stress of ER fluids decreased as the temperature increased, which is ascribed to the reduction of both zero-field viscosity and dielectric constant of silicone oil with rising temperature.[40,41] On the contrary, the yield stress was enhanced with increasing temperature under an electric field (Figure 7b). Even though Brownian motion was intensified due to the increased temperature, the Brownian force could be overcome by the increased interparticle interaction force which was ascribed to the enhanced interfacial polarization.[42] The enhancement of interfacial polarization is related to the dielectric constant of ER fluids. It has been reported that the dielectric constant of ER fluids generally increased with rising temperature, which is associated with the enhancement of interfacial polarization with increasing temperature under an electric field.[43,44] Furthermore, the viscosity of silicone oil which was utilized as a medium decreased with rising temperature, which makes it easy for ER materials to form fibril-like structure under an electric field.[42] For the reasons mentioned above, the yield stress of ER fluids was enhanced with increasing temperature. This tendency was observed for all ER fluids prepared in this work. Namely, the fabricated ER fluids composed of double-shell $SiO_2/TiO_2$ hollow nanoparticles exhibited excellent and stable performance over a wide range of temperature.

**TABLE 4. Physical Parameters and Sedimentation Velocity of DS HNPs**

| particle size[a] | 120 nm | 150 nm | 180 nm | 240 nm |
|---|---|---|---|---|
| particle density[b] | 2.68 g $cm^{-3}$ | 2.70 g $cm^{-3}$ | 2.71 g $cm^{-3}$ | 2.74 g $cm^{-3}$ |
| fluid density[c] | 1.01 g $cm^{-3}$ | 1.01 g $cm^{-3}$ | 1.01 g $cm^{-3}$ | 1.01 g $cm^{-3}$ |
| fluid viscosity[c] | 0.101 Pa.s | 0.101 Pa.s | 0.101 Pa.s | 0.101 Pa.s |
| sedimentation velocity[d] | $1.30 \times 10^{-10}$ m $s^{-1}$ | $2.05 \times 10^{-10}$ m $s^{-1}$ | $2.97 \times 10^{-10}$ m $s^{-1}$ | $5.37 \times 10^{-10}$ m $s^{-1}$ |

[a] The average particle size was confirmed by TEM (50 particles counted). [b] Particle density was measured using a density hydrometer at a standard temperature of 20 °C. [c] Silicone oil [poly(methylphenylsiloxane), kinetic viscosity = 100 cSt] was used as a dispersing medium. [d] Sedimentation velocity was determined according to Stokes law. Particle Reynolds number was less than 0.2.'

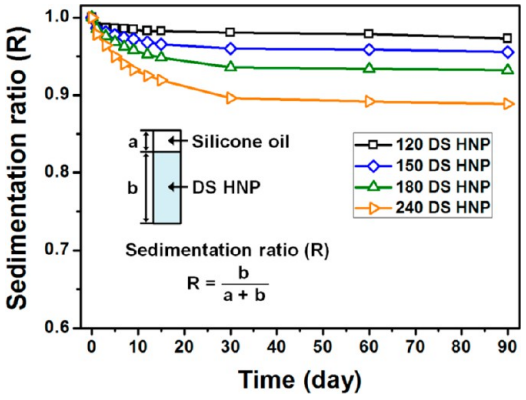


**Figure 8. Sedimentation properties of the DS HNPs-based ER fluids with four different diameters (120, 150, 180, and 240 nm). Concentration of the ER fluilds was 10 wt% in silicone oil [inset: definition of sedimentation ratio].**

Particularly, the DS HNPs dispersed in silicone oil exhibited an outstanding antisedimentation property because of their low density ascribed to the hollow structure (Figure 8). The sedimentation ratio was maintained above 0.88 even after ninety days. It is noteworthy that the antisettling property was improved as the diameter of DS HNPs decreased. To evaluate the antisedimentation property of the DS HNPs mathematically, sedimentation velocity of the DS HNPs was determined by using the Stokes' law as follows:

$$V_g = d^2(\rho_p - \rho_l)/18\eta \times G$$

where $V_g$ is sedimentation velocity, $d$ is particle diameter, $\rho_p$ is particle density, $\rho_l$ is liquid density, $\eta$ is liquid viscosity, and $G$ is gravitational acceleration.[45,46] As described in Table 4, the sedimentation velocities of DS HNPs were remarkably low. Judging from the calculated sedimentation velocities of DS HNPs, the small-sized DS HNPs showed superior antisedimentation behavior.

## CONCLUSION

In summary, DS HNPs were successfully fabricated to examine the influence of the shell structure of ER materials on ER properties. The DS HNPs-based ER fluids exhibited significantly enhanced ER performance compared with the SS HNPs-based ER fluids. Particularly, the DS HNPs-based ER fluid showed the yield stress value of *ca.* 45.5 kPa, which was 4.1-fold higher than that of same weight fraction of the SS HNPs-based ER fluid. The improvement of ER activities was explained by pore structure and distribution. Because of the interfacial polarization produced by the increased number of shells, the DS HNPs-based ER fluid represented higher yield stress under an applied electric field. In addition, the ER performance of the DS HNPs-based ER fluids was observed to increase with a decrease in the diameter of particles, which was attributed to the increased surface area of the shell but not the small pores within shells. The yield stress of DS HNPs-based ER fluids was improved by 6.6 times as the diameter of DS HNPs was reduced by half. The enhanced achievable polarizability of the smaller DS HNPs was also confirmed by measuring the dielectric parameters of the DS HNPs. Moreover, the DS HNPs-based ER fluids represent outstanding antisettling properties, which promise a sufficient potential for practical and commercial applications.

## MATERIALS AND METHODS

**Fabrication of Double-Shell $SiO_2/TiO_2$ Hollow Nanoparticles.** Silica nanoparticles of various sizes were prepared using the Stöber method.[47] Titanium (IV) isopropoxide (TTIP) was dropped into the colloidal solution of silica nanoparticles, blended with 18 mL of ethanol, and 6 mL of acetonitrile. This colloidal solution reacted at 4 °C for 6 h to obtain $SiO_2/TiO_2$ core/shell nanoparticles (ST CS NPs). The reacted solution was centrifuged for 20 min at 12 000 rpm and dispersed in deionized water (80 mL). The solution containing the ST CS NPs was stirred with polyvinylpyrrolidone (PVP, $M_w$ of 1 300 000) for 12 h to coat PVP onto the surface of the ST CS NPs. The PVP-coated ST CS NPs were centrifuged and redispersed in ethanol (158 mL). The ST CS NPs solution was mixed with 2 mL of ammonia solution and 1.4 mL of deionized water. Tetraethyl orthosilicate (TEOS, 5.8 mL) was dropped to the ST CS NPs solution and stirred for 4 h to coat silica onto the surface of the ST CS NPs surface. A solution of silica-coated ST CS NPs (STS CS NPs) was mixed with 5.8 mL of TTIP, 9 mL of ethanol, and 3 mL of acetonitrile. $SiO_2/TiO_2/SiO_2/TiO_2$ core/shell nanoparticles (STST CS NPs) were produced by sol–gel reaction of this solution. The DS HNPs were obtained *via* etching and redeposition process using sonication with 0.1 M ammonia solution.[27] The final products were acquired by centrifugation of the solution at 12 000 rpm for 10 min and washing with ethanol twice.

**Analysis of Electrorheological Properties.** Dried particles were dispersed in silicone oil (poly(methylphenylsiloxane), viscosity = 100 cSt) and stirred with magnetic stirrer to disperse the particles uniformly. Concentration of the ER fluids was 10 wt% and no additives were added into the ER fluid. All ER fluids were prepared by the same method. ER properties of the prepared fluids were measured using rheometer (AR 2000 Advanced Rheometer, TA Instrument) with a concentric cylinder conical geometry, a temperature controller, and a high voltage generator (Trek 677B). The gap distance between the cup and rotor was 1.00 mm and the ER fluid was placed in that space. To get an equilibrium chainlike structure, an electric field was applied for 3 min before starting measurement. All measurements were performed at room temperature.

**Characterization.** Transmission electron microscopy (TEM) images were acquired by a JEM-2100 (JEOL) installed at the National Center for Inter-university Research Facilities (NCIRF) at Seoul National University. Total surface area and pore distribution were examined using a Micromeritics analyzer (ASAP 2000; Micromeritics Co., Norcross, GA). Elemental composition of the particles were obtained using elemental analyzer (EA1110, CE Instrument) and Inductively Coupled Plasma-Atomic Emission Spectrometer (ICPS-7500, SHIMADZU Corporation, Japan). Scanning transmission electron microscopy (STEM)-energy dispersive spectroscopy (EDS) elemental maps were acquired using STEM (Tecnai F20, FEI) equipped with a Gatan image filter (Gatan, Inc.). The ER properties were measured using a rheometer (AR 2000 Advanced Rheometer, TA Instruments) having a concentric cylinder conical geometry with a cup radius of 15 mm, a temperature controller, and a high-voltage generator (Trek 677B). The dielectric spectra of the ER fluids were acquired by an impedance analyzer (1260, Solartron) combined with a dielectric interface (1296, Solartron).

More detailed characterization on pore volume distribution is presented in the Supporting Information.

*Conflict of Interest:* The authors declare no competing financial interest.

*Supporting Information Available:* Pore volume distributions derived from the desorption isotherms; elemental analysis; electrorheological properties at zero field condition. This material is available free of charge via the Internet at http://pubs.acs.org.

*Note Added after ASAP Publication:* This paper was published ASAP April 8, 2015. Due to a production error, an extraneous character was introduced to the equation defining $A_{shell}$. The corrected version was reposted April 20, 2015.

## REFERENCES AND NOTES


1. Hong, J. Y.; Jang, J. A Comparative Study on Electrorheological Properties of Various Silica-Conducting Polymer Core−Shell Nanospheres. *Soft Matter* **2010**, *6*, 4669–4671.
2. Hao, T. Electrorheological Fluids. *Adv. Mater.* **2001**, *13*, 1847–1857.
3. Grzelczak, M.; Vermant, J.; Furst, E. M.; Liz-Marzán, L. M. Directed Self-Assembly of Nanoparticles. *ACS Nano* **2010**, *4*, 3591–3605.
4. Fang, F. F.; Choi, H. J.; Ahn, W.-S. Electrorheology of a Mesoporous Silica Having Conducting Polypyrrole inside Expanded Pores. *Microporous Mesoporous Mater.* **2010**, *130*, 338–343.
5. Yin, J.; Zhao, X.; Xiang, L.; Xia, X.; Zhang, Z. Enhanced Electrorheology of Suspensions Containing Sea-Urchin-like Hierarchical Cr-Doped Titania Particles. *Soft Matter* **2009**, *5*, 4687–4697.
6. Hong, J. Y.; Kwon, E.; Jang, J. Fabrication of Silica/Polythiophene Core/Shell Nanospheres and Their Electrorheological Fluid Application. *Soft Matter* **2009**, *5*, 951–953.
7. Sedlačík, M.; Mrlík, M.; Pavlínek, V.; Sáha, P.; Quadrat, O. Electrorheological Properties of Suspensions of Hollow Globular Titanium Oxide/Polypyrrole Particles. *Colloid Polym. Sci.* **2012**, *290*, 41–48.
8. Sung, B. H.; Choi, U. S.; Jang, H. G.; Park, Y. S. Novel Approach To Enhance the Dispersion Stability of ER Fluids Based on Hollow Polyaniline Sphere Particle. *Colloids Surf. A* **2006**, *274*, 37–42.
9. Cheng, Q.; Pavlinek, V.; He, Y.; Yan, Y.; Li, C.; Saha, P. Synthesis and Electrorheological Characteristics of Sea Urchin-Like $TiO_2$ Hollow Spheres. *Colloid Polym. Sci.* **2011**, *289*, 799–805.
10. Halsey, T. C. Electrorheological Fluids—Structure and Dynamics. *Adv. Mater.* **1993**, *5*, 711–718.
11. Hong, J. Y.; Choi, M.; Kim, C.; Jang, J. Geometrical Study of Electrorheological Activity with Shape-Controlled Titania-Coated Silica Nanomaterials. *J. Colloid Interface Sci.* **2010**, *347*, 177–182.
12. Yin, J. B.; Zhao, X. P. Preparation and Enhanced Electrorheological Activity of $TiO_2$ Doped with Chromium Ion. *Chem. Mater.* **2004**, *16*, 321–328.
13. Shin, K.-Y.; Lee, S.; Hong, S.; Jang, J. Graphene Size Control *via* a Mechanochemical Method and Electroresponsive Properties. *ACS Appl. Mater. Interfaces* **2014**, *6*, 5531–5537.
14. Sim, I. S.; Kim, J. W.; Choi, H. J.; Kim, C. A.; Jhon, M. S. Preparation and Electrorheological Characteristics of Poly(*p*-phenylene)-Based Suspensions. *Chem. Mater.* **2001**, *13*, 1243–1247.
15. Cho, M. S.; Choi, H. J.; Jhon, M. S. Shear Stress Analysis of a Semiconducting Polymer Based Electrorheological Fluid System. *Polymer* **2005**, *46*, 11484–11488.
16. Liu, Y. D.; Choi, H. J. *Soft Matter* **2012**, *8*, 11961–11978.
17. Hong, J. Y.; Lee, E.; Jang, J. Electro-responsive and Dielectric Characteristics of Graphene Sheets Decorated with $TiO_2$ Nanorods. *J. Mater. Chem. A* **2013**, *1*, 117–121.
18. Yin, J. B.; Zhao, X. P. Preparation and Electrorheological Activity of Mesoporous Rare-Earth-Doped $TiO_2$. *Chem. Mater.* **2002**, *14*, 4633–4640.
19. Vemuri, S. H.; Jhon, M. S.; Zhang, K.; Choi, H. J. New Analysis of Yield Stress on Giant Electrorheological Fluids. *Colloid Polym. Sci.* **2012**, *290*, 189–192.
20. Zhang, K.; Liu, Y. D.; Jhon, M. S.; Choi, H. J. Generalized Yield Stress Equation for Electrorheological Fluids. *J. Colloid Interface Sci.* **2013**, *409*, 259–263.
21. Parthasarathy, M.; Klingenberg, D. J. Electrorheology: Mechanisms and Models. *Mater. Sci. Eng. R-Rep.* **1996**, *17*, 57–103.
22. Liu, Y. D.; Cheng, Y.; Xu, G.; Choi, H. J. Yield Stress Analysis of 1D Calcium and Titanium Precipitate-Based Giant Electrorheological Fluids. *Colloid Polym. Sci.* **2013**, *291*, 1267–1270.
23. Huang, X.; Wen, W.; Yang, S.; Sheng, P. Mechanisms of the Giant Electrorheological Effect. *Solid State Commun.* **2006**, *139*, 581–588.
24. Wen, W.; Huang, X.; Yang, S.; Lu, K.; Sheng, P. The Giant Electrorheological Effect in Suspensions of Nanoparticles. *Nat. Mater.* **2003**, *2*, 727–730.
25. Lee, S.; Hong, J. Y.; Jang, J. Synthesis and Electrical Response of Polyaniline/Poly(styrene sulfonate)-Coated Silica Spheres Prepared by Seed-Coating Method. *J. Colloid Interface Sci.* **2013**, *398*, 33–38.
26. Chen, Z. H.; Kim, C.; Zeng, X. B.; Hwang, S. H.; Jang, J.; Ungar, G. Characterizing Size and Porosity of Hollow Nanoparticles: SAXS, SANS, TEM, DLS, and Adsorption Isotherms Compared. *Langmuir* **2012**, *28*, 15350–15361.
27. Choi, M.; Kim, C.; Ok Jeon, S.; Soo Yook, K.; Yeob Lee, J.; Jang, J. Synthesis of Titania Embedded Silica Hollow Nanospheres *via* Sonication Mediated Etching and Redeposition. *Chem. Commun.* **2011**, *47*, 7092–7094.
28. Zhang, T.; Ge, J.; Hu, Y.; Zhang, Q.; Aloni, S.; Yin, Y. Formation of Hollow Silica Colloids through a Spontaneous Dissolution-Regrowth Process. *Angew. Chem., Int. Ed.* **2008**, *47*, 5806–5811.
29. Park, S. J.; Kim, Y. J.; Park, S. J. Size-Dependent Shape Evolution of Silica Nanoparticles into Hollow Structures. *Langmuir* **2008**, *24*, 12134–12137.
30. Choi, H. J.; Hong, C. H.; Jhon, M. S. Cole−Cole Analysis on Dielectric Spectra of Electrorheological Suspensions. *Int. J. Mod. Phys. B* **2007**, *21*, 4974–4980.

31. Hao, T.; Kawai, A.; Ikazaki, F. Mechanism of the Electrorheological Effect: Evidence from the Conductive, Dielectric, and Surface Characteristics of Water-Free Electrorheological Fluids. *Langmuir* **1998**, *14*, 1256–1262.
32. Lee, S.; Yoon, C.-M.; Hong, J.-Y.; Jang, J. Enhanced Electrorheological Performance of a Graphene Oxide-Wrapped Silica Rod with a High Aspect Ratio. *J. Mater. Chem. C* **2014**, *2*, 6010–6016.
33. Asami, K. Characterization of Heterogeneous Systems by Dielectric Spectroscopy. *Prog. Polym. Sci.* **2002**, *27*, 1617–1659.
34. Kim, S. D.; Zhang, W. L.; Choi, H. J. Pickering Emulsion-Fabricated Polystyrene−Graphene Oxide Microspheres and Their Electrorheology. *J. Mater. Chem. C* **2014**, *2*, 7541–7546.
35. Kim, K.; Stroud, D.; Li, X.; Bergman, D. J. Method to Calculate Electrical Forces Acting on a Sphere in an Electrorheological Fluid. *Phys. Rev. E* **2005**, *71*, 031503.
36. Kim, S.; Kim, C.; Hong, J.-Y.; Hwang, S. H.; Jang, J. Enhanced Electrorheological Performance of Barium-Doped $SiO_2$/$TiO_2$ Hollow Mesoporous Nanospheres. *RSC Adv.* **2014**, *4*, 6821–6824.
37. Gamota, D. R.; Schubring, A. W.; Mueller, B. L.; Filisko, F. E. Amorphous Ceramics as the Particulate Phase in Electrorheological Materials Systems. *J. Mater. Res.* **1996**, *11*, 144–155.
38. Wang, B. X.; Zhao, X. P. Wettability of Bionic Nanopapilla Particles and Their High Electrorheological Activity. *Adv. Funct. Mater.* **2005**, *15*, 1815–1820.
39. Liu, Y. D.; Quan, X.; Hwang, B.; Kwon, Y. K.; Choi, H. J. Core−Shell-Structured Monodisperse Copolymer/Silica Particle Suspension and Its Electrorheological Response. *Langmuir* **2014**, *30*, 1729–1734.
40. Conrad, H.; Sprecher, A. F.; Choi, Y.; Chen, Y. The Temperature Dependence of the Electrical Properties and Strength of Electrorheological Fluids. *J. Rheol.* **1991**, *35*, 1393–1410.
41. Kim, S. G.; Lim, J. Y.; Sung, J. H.; Choi, H. J.; Seo, Y. Emulsion Polymerized Polyaniline Synthesized with Dodecylbenzene-Sulfonic Acid and Its Electrorheological Characteristics: Temperature Effect. *Polymer* **2007**, *48*, 6622–6631.
42. Yin, J.; Xia, X.; Xiang, L.; Zhao, X. Temperature Effect of Electrorheological Fluids Based on Polyaniline Derived Carbonaceous Nanotubes. *Smart Mater. Struct.* **2011**, *20*, 015002.
43. Zhao, X. P.; Yin, J. B. Preparation and Electrorheological Characteristics of Rare-Earth-Doped $TiO_2$ Suspensions. *Chem. Mater.* **2002**, *14*, 2258–2263.
44. Yin, J.; Zhao, X. Temperature Effect of Rare Earth-Doped $TiO_2$ Electrorheological Fluids. *J. Phys. D: Appl. Phys.* **2001**, *34*, 2063–2067.
45. Lee, S.; Hong, J.-Y.; Jang, J. Performance Enhancement of White Light-Emitting Diodes Using an Encapsulant Semi-Solidification Method. *J. Mater. Chem. C* **2014**, *2*, 8525–8531.
46. Yoon, C.-M.; Lee, S.; Hong, S. H.; Jang, J. Fabrication of Density-Controlled Graphene Oxide-Coated Mesoporous Silica Spheres and Their Electrorheological Activity. *J. Colloid Interface Sci.* **2014**, *438*, 14–21.
47. Stöber, W.; Fink, A.; Bohn, E. Controlled Growth of Monodisperse Silica Spheres in the Micron Size Range. *J. Colloid Interface Sci.* **1968**, *26*, 62–69.